Accelerated MR Parameter Mapping Using Robust Model-Consistency Reconstruction

Alexey Samsonov[1]
[1]*University of Wisconsin, Madison, Wisconsin, United States*

INTRODUCTION: MR parameter mapping may offer more sensitive and specific imaging markers than conventional MRI (1). Standard parameter mapping procedure consists of acquisition of several *k*-space datasets at multiple values of pulse sequence parameters (i.e., echo time in T2 mapping), followed by image series reconstruction and subsequent voxel-wise fit by a (typically non-linear) signal model. The scan time penalty associated with parametric dimension sampling often requires undersampling of individual *k*-space datasets at levels which are beyond capabilities of standard reconstruction techniques such as parallel MRI. An appealing reconstruction strategy in such cases is to utilize *k*-space data and analytical signal models jointly to estimate parameter maps directly from *k*-space data (2) or to improve reconstruction of the image series (3-5). In such techniques, solution is sought among the set of functions that strictly satisfy the chosen model, be it the original nonlinear signal model (2,6) or its linearized forms (3-5). In practice, however, the model-based strategy may lead to sub-optimal performance because actual signal may deviate from the model in many voxels (e.g., due to modeling simplifications, partial voluming, motion, etc). In this work, we propose a new model-based reconstruction technique, whose intrinsic insensitivity to the model mismatch in such voxels results in improved reconstruction of MR parameter maps.

THEORY: Let $\bar{\mathbf{f}} = [\mathbf{f}_1 \ \ldots \ \mathbf{f}_N]^T$ be a vector containing a parametric image series, whose dependence on model parameters $\bar{\mathbf{p}}$ is described by an analytical signal model $\bar{\mathbf{f}} = S(\bar{\mathbf{p}})$. Let $\bar{\mathbf{p}} = \tilde{S}(\bar{\mathbf{f}})$ be its adjoint operator mapping an image series to the corresponding parametric maps (e.g., using voxel-wise model fit). If $\bar{\mathbf{f}}$ is consistent with the signal model, condition $\mathbf{P}\bar{\mathbf{f}} \equiv S(\tilde{S}(\bar{\mathbf{f}})) \equiv \bar{\mathbf{f}}$ (Eq. [1]) should hold. In accelerated imaging, $\bar{\mathbf{f}}$ has to be obtained from a poorly conditioned matrix equation $\bar{\mathbf{E}}\bar{\mathbf{f}} = \bar{\mathbf{s}}$, where $\bar{\mathbf{E}}$ is the encoding matrix and $\bar{\mathbf{s}}$ is all measured *k*-space data. As proposed in (4), both model consistency and data consistency terms may be combined into a joint constrained problem: $\min_{\bar{\mathbf{f}}} \left\| \mathbf{P}\bar{\mathbf{f}} - \bar{\mathbf{f}} \right\|_1$ *subject to* $\left\| \bar{\mathbf{E}}\bar{\mathbf{f}} - \bar{\mathbf{s}} \right\|_2 < \varepsilon$ (Eq. [2]), where $\|\cdot\|_{1/2}$ are l_1/l_2 norms, respectively, and ε is chosen according to the noise level. The use of l_1 norm in the model-consistency term allows avoiding excessive penalization of signals deviating from the model. The previous efforts to solve this l_1 problem via linearization of the model-consistency operator $\mathbf{P}$ (4) introduced significant reconstruction errors due to linearization.(7). Here, we develop a new algorithm to solve the l_1-problem of Eq. [2] which allows utilization of nonlinear models. We generate a sequence of iterates by alternating the gradient descent update of solution and a model projection operator to satisfy both data and model consistency, respectively. This sequence is conceptually related to the projected gradients (PG) approach (8), with a projection designed to apply the MOdel-Consistency COndition (MOCCO) (Eq. [1]) in robust (l_1) fashion. The resulting algorithm (PG-MOCCO$_1$) is shown on the right. To provide robustness to the model mismatch, the model consistency update is performed using reweighting matrix $\mathbf{W}_1$ designed to enforce l_1 behavior of the model-consistency term (Eq. [1]).

PG-MOCCO$_1$ Algorithm:

Set $\bar{\mathbf{f}}^{(0)}, \beta_0 < 1, n = 0, \sigma_0, \alpha$

ST_1: $\bar{\mathbf{f}}_d^{(n+1)} = \bar{\mathbf{f}}^{(n)} + \alpha \bar{\mathbf{E}}^H \left(\bar{\mathbf{s}} - \bar{\mathbf{E}}\bar{\mathbf{f}}^{(n)} \right)$

ST_2: $\Delta_m^{(n+1)} = \mathbf{P}\bar{\mathbf{f}}_d^{(n+1)} - \bar{\mathbf{f}}_d^{(n+1)}$

ST_3: $\sigma = \sigma_0 std\left(\Delta_m^{(n+1)}\right)(\beta_0)^n$

ST_4: $\mathbf{W}_1 = 1 \Big/ \sqrt{\left(\Delta_m^{(n+1)} / \sigma\right)^2 + 1}$

ST_5: $\bar{\mathbf{f}}^{(n+1)} = \bar{\mathbf{f}}_d^{(n+1)} + \mathbf{W}_1 \Delta_m^{(n+1)}$

Converged ? Yes : $\bar{\mathbf{p}} = \tilde{S}(\bar{\mathbf{f}})$; *No :* ST_1

METHODS: PG-MOCCO$_1$ algorithm was compared to the model-based direct parameter mapping (DPM) method of Block et al (2), which finds $\bar{\mathbf{p}}$ from *k*-space data by solving $\min_{\bar{\mathbf{p}}} \left\| \bar{\mathbf{E}}S(\bar{\mathbf{p}}) - \bar{\mathbf{s}} \right\|_2$. Multi-spin-echo data were simulated using discrete (no partial voluming (PV)) and fuzzy (with PV) brain models from BrainWeb online database (8) (32 echoes, 8.4 ms echo spacing, TR=1.5s). Additionally, in-vivo data were collected on a 3T clinical MRI (MR750w, GE Healthcare, Waukesha, WI) using 8-ch array (16 echoes, 8.4 ms spacing, FOV 220×220 mm, 6-mm slice, 256×256 matrix, TR=1.5s). The data were then combined into a single coil channel using the method of Walsh et al (9). Both simulated and in-vivo data were retrospectively undersampled using 2D variable density randomized trajectory (reduction factor *R*=3.5 for 32-echo simulated data, and *R*=2.5 for 16-echo in-vivo data). Standard single-exponential T2 model was used in the algorithms. The normalized root-mean-squared error (nRMSE) relative to the groundtruth images or R2=1/T2 maps was used to assess the methods' performance.

RESULTS: Figure 1 compares the methods' performances on simulated T2 data. While they are similar for discrete model, introduction of PV voxels precludes full convergence of the global optimization in DPM. PG-MOCCO$_1$ also relies on a single-exponential model to describe signal evolution in all voxels including PV ones; however, its robust formulation leads to smaller nRMSE. Figure 2 further demonstrates improved ability of PG-MOCCO$_1$ to handle model mismatch (Fig. 2a). In this case, DPM reconstruction results not only in PV voxel errors but also in increased overall image error, which reduces overall quality of DPM R2 map compared to groundtruth and PG-MOCCO$_1$ (Fig. 2b). Figure 3 demonstrates the methods' performance on in-vivo T2 datasets. Fitting the T2 decay model to fully sampled images reveals inconsistency of the model within the vessels, especially for the slice in the right pane. While PG-MOCCO$_1$ reduces R2 error more efficiently compared to DPM for both slices, its robustness makes the improvements most evident in the "poor" model fit case (note different error scales for left and right panes in Fig. 3).

DISCUSSION: We presented a novel method (PG-MOCCO$_1$) to reconstruct parametric maps from data sampled below the Nyquist limit. Similar to other methods for accelerated MR parameter mapping, our algorithm utilizes nonlinear models to limit the solution space. However, PG-MOCCO$_1$ is more resilient to deficiencies in signal representation by such models resulting in significant gains in reconstruction accuracy. This may be explained by the fact that it avoids hard constraining to the models. Instead, it relies on l_1 norm in its formulation which provides robustness to outliers. Because the optimization problem is solved globally in DPM approaches, the presence of such outliers causes incomplete convergence and decreased accuracy of parameter estimation not only in these voxels but also in other image areas.

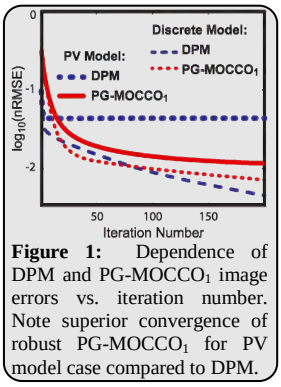

Figure 1: Dependence of DPM and PG-MOCCO$_1$ image errors vs. iteration number. Note superior convergence of robust PG-MOCCO$_1$ for PV model case compared to DPM.

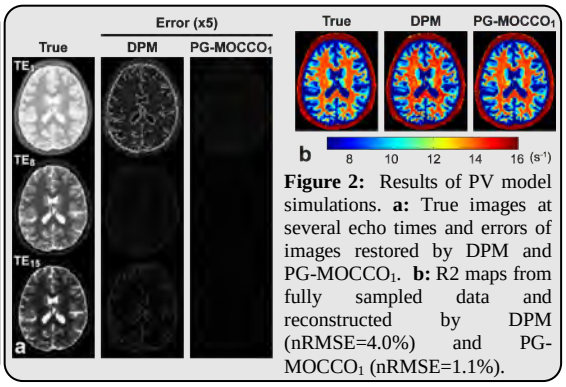

Figure 2: Results of PV model simulations. **a:** True images at several echo times and errors of images restored by DPM and PG-MOCCO$_1$. **b:** R2 maps from fully sampled data and reconstructed by DPM (nRMSE=4.0%) and PG-MOCCO$_1$ (nRMSE=1.1%).

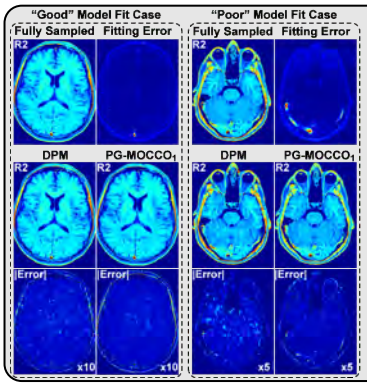

Figure 3: R2 mapping using DPM and PG-MOCCO$_1$. Slice in Left Pane is fit better by the model than slice in Right Pane. Error levels are visually similar for "good" model fit (left). Stronger mismatch of data and model for "poor" model fit case causes DPM to underperform (degradation of cerebellum structures and increased image errors). Note that DPM error is spread across R2 map.

REFERENCES: [1] Alexander AL, et al. Brain Connect 2011;1:423. [2] Block KT, et al, IEEE TMI 2009;28:1759. [3] Doneva M, et al. MRM 2010;64:1114. [4] Samsonov A. ISMRM 2012, p. 358. [5] Huang C, et al. MRM 2012;67:1355. [6] Tran-Gia J, et al. MRM 2013;70:1524. [7] Samsonov A, SFB Workshop, 2014 Graz, Austria. [8] Collins DL, et al. IEEE TMI 1998;17;463. [9] Walsh DO, et al. MRM 2000:43:682.

ACKNOWLEDGEMENTS: This work was supported by NIH (R01NS065034, R21EB018483).